DE GRUYTER Adv. Opt. Techn. 2016; 5(2): 177–186

Research Article

Krste Pangovski*, Martin Sparkes and William O'Neill

A holographic method for optimisation of laser-based production processes

DOI 10.1515/aot-2015-0057
Received December 1, 2015; accepted March 8, 2016

Abstract: A digital holographic system is used to image the plume dynamics of a train of picosecond laser pulses interacting with titanium, aluminium, copper and brass. The recorded process dynamics are used to propose two optimisation strategies: first, by observing the time at which the plume fully dissipates and, second, through calculation of the minimum beam displacement required to maximise energy delivery to the sample by avoiding the plume. The proposed approach could further be applied in real industrial process design, allowing laser users to formulate a processing strategy based on process dynamics rather than lengthy post-process evaluation of a sample.

Keywords: holographic diagnostics; laser-materials processing; plume dynamics; process optimisation.

1 Introduction

It is easy to appreciate the startling advances in industrial laser design; in recent years, laser designers have improved beam quality to the diffraction limit while at the same time increasing the available power. Development of new laser technologies is being driven by industrial demand for high repetition rate, high beam quality, and high average/peak power. Lasers have come in leaps and bounds since the demonstration of the first operational laser and continue to gain market share in many established areas, while challenging conventional technology, traditionally outside the scope of these laser systems. More recently, the introduction of high-performance short-pulse systems with repetition rates in the MHz range have provided the user with an even wider parameter range. Despite this, laser process design remains heavily reliant on empirical evidence, partly because of the vast parameter space available across the laser industry, where modern lasers offer near infinite choice of parameters (wavelength, pulse energy, pulse duration, repetition rate, polarisation, beam quality parameter M^2, etc.) in any practical terms. In this work, we propose a novel methodology based on pulsed digital holography that provides industrial laser users with quantitative data for process optimisation.

2 Theoretical background

2.1 Laser-material dynamics

Laser-matter interactions are complex and take place via several key mechanisms associated with the range of time scales spanning some 15 orders of magnitude, shown in Figure 1. Early times are characterised by energy absorption into the material with characteristic timescales of 10^{-15} s. Plasma initiation occurs on the picosecond (10^{-12} s) timescale, while vaporisation and melting are inherently thermal processes and are delayed in their response by the characteristic energy-lattice transfer time. Shockwave emissions are long-lived with typical timescales ranging from 10^{-12} s to more than 10^{-3} s. Although many laser-induced shockwaves take on a spherical form [1, 2], many other geometries have been observed in the form of jet-like structures [3] or where multiple shockwave centres are present [4] and are typically dependent on the gas present during processing [5].

Material ejection via vaporisation can be seen as early as a few hundred picoseconds after pulse impact, while melt ejection from the bulk has a delayed response. In the case of phase explosions, this can occur several hundred

---

***Corresponding author: Krste Pangovski,** Centre for Industrial Photonics, Institute for Manufacturing, University of Cambridge, CB30FS, UK, e-mail: kp358@cam.ac.uk
Martin Sparkes and William O'Neill: Centre for Industrial Photonics, Institute for Manufacturing, University of Cambridge, CB30FS, UK

www.degruyter.com/aot

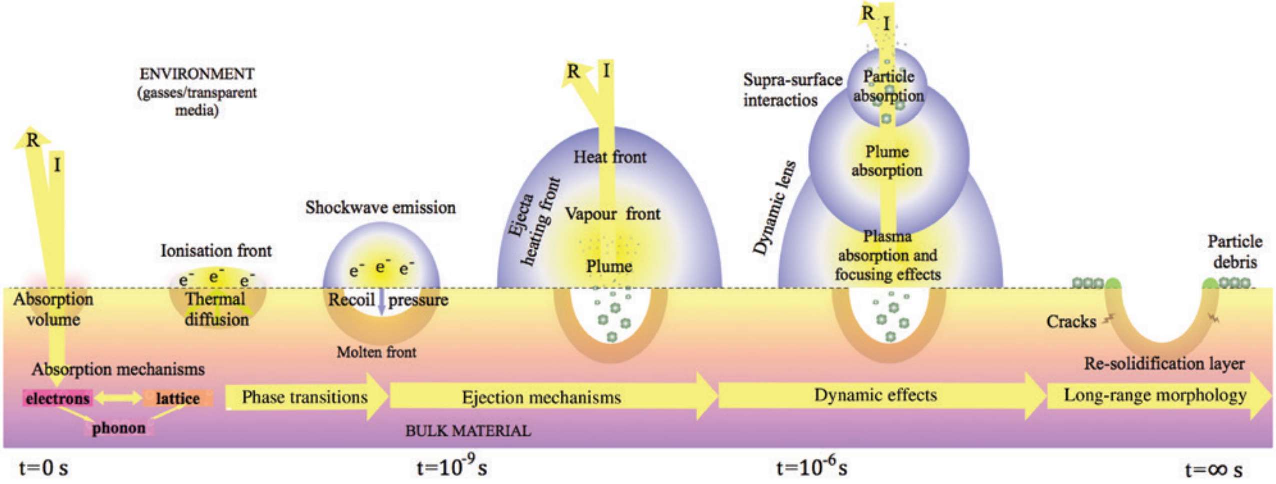

Figure 1: Interaction mechanisms and associated timescales.

nanoseconds after pulse impact [6, 7]. In the nanosecond regime, thermal and structural events dominate: although the energy may be delivered in a few picoseconds or less, the material continues to experience thermal and structural changes for many microseconds, which is often within the processing window of subsequent pulses. Energy coupling into the material depends strongly on material properties such as reflectivity and absorptivity and also on material preparation, which determine factors such as surface quality.

The induced shock wave, plume and plasma form a heat source at the processing zone, which interacts with the remainder of the incident (and subsequent) laser pulses [4]. Onset of these phenomena leads to secondary energy coupling with molten ejecta, vapour or plasma [4, 8] that can have a profound effect on the dynamics of the interaction as well as the final morphology of the affected site. It is, therefore, useful to diagnose and define a process by the dynamics that it undergoes, as this is a unique fingerprint, and can be accomplished through use of digital holography.

2.2 Digital holographic interferometry

One of the most powerful diagnostic techniques for high-power laser-matter interaction is digital holographic interferometry (DHI). Unlike conventional high-speed photographs, a hologram records both the phase and amplitude of a wave field and can be extracted by observing the interference fringes arising from a diffracted or scattered wave field, and a coherent background. The interference process is described by the well-known expression:

$$\begin{aligned} I(x,y) &= |O(x,y)+R(x,y)|^2 \\ &= |O(x,y)|^2+|R(x,y)|^2 \\ &\quad +O(x,y)R^*(x,y)+R(x,y)O^*(x,y) \\ &= R(x,y)R^*(x,y)+O(x,y)O^*(x,y) \\ &\quad +O(x,y)R^*(x,y)+R(x,y)O^*(x,y) \end{aligned} \tag{1}$$

where * denotes the complex conjugate and

$$O(x,y)=o(x,y)e^{i\varphi_0(x,y)} \tag{2}$$

and

$$R(x,y)=r(x,y)e^{i\varphi_r(x,y)} \tag{3}$$

are the complex amplitudes of the probe (or object) and reference wave fronts. Here, $o(x, y)$ and $r(x, y)$ are the real amplitudes of the probe and reference waves, while $e^{i\varphi_0(x,y)}$ and $e^{i\varphi_r(x,y)}$ are the phase terms. A typical holographic imaging system is depicted in Figure 2. A coherent beam is split into an object and reference arms and is recombined at the surface of the recording device.

The resulting interference pattern $I(x, y)$ – a hologram – may be recorded using photographic film or more recently by digital means, as first demonstrated by Goodman [9] on CCD, CMOS or ICCD chips, and can then be digitally manipulated. A hologram can be recorded with a wide range of optical configurations that can be classed into two main categories: in-line and off-axis holography. The original in-line configuration was mired by direct current (DC) noise owing to the overlap between the object and reference wave fields. Major improvements to image quality were realised with the introduction of off-axis geometries [10]. In this configuration, the noise from the DC term $|O(x, y)|^2+|R(x, y)|^2$ was spatially separated from the

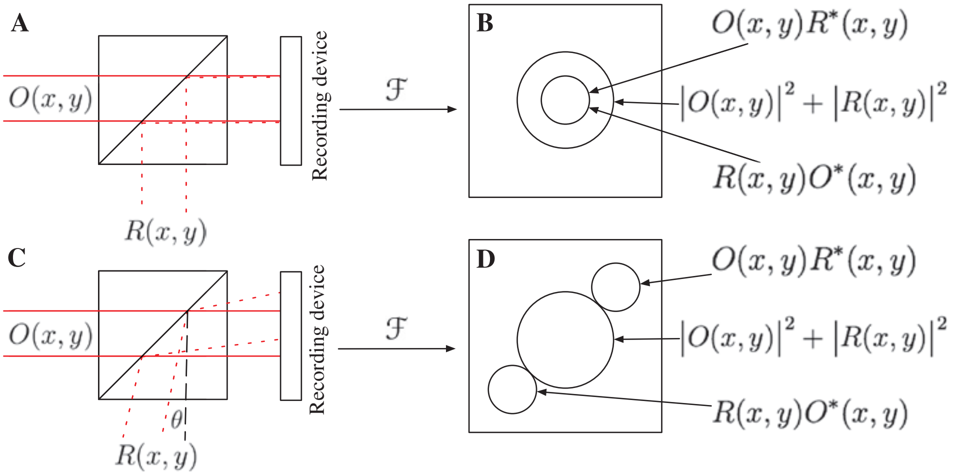

Figure 2: (A) The recombination optics of an in-line geometry, (B) the spatial frequency representation of the recorded hologram with the zero order and side lobes occupying the same space, (C) the recording in off-axis configuration and (D) spatial frequency representation of off-axis holograms with the zero order and the side lobes separated. $\mathcal{F}$ represents a Fourier transform.

side orders $O(x, y)R^*(x, y)+R(x, y)O^*(x, y)$ that contain the information about the object under examination. Figure 2 shows the benefit of employing off-axis geometries.

Whenever a laser pulse ablates a material, the pressure created immediately above the event results in a shockwave or plasma that manifests as refractive index variations that can be detected by holographic means; when a photon passes through an area of differing refractive index in transparent media, the optical path length results in a relative phase change. Any refractive index change in a transparent medium will lead to change in the optical path length experienced by the wave, leading to a phase difference with a wave that has not propagated through the disturbed medium. In this way, it is possible to detect path-length variations as low as $\lambda/100$ [11].

Recombining these waves using a system depicted in Figure 2 gives rise to interference fringes that contain information about the refractive index change. This interference pattern is then digitally manipulated to provide refractive index information. The phase change due to variations in the refractive index is given by [12–14]:

$$\Delta\varphi(x, y)=\frac{2\pi}{\lambda}\int_0^d [n(x, y, z)-n_0]dz \tag{4}$$

where λ is the probe wavelength, n_0 is the refractive index of the unperturbed medium and $n(x, y, z)-n_0$ is the refractive index change. As phase changes are additive, the integral accounts for variations throughout the object. Knowledge of refractive index enables extraction of several key parameters (such as shockwave or plasma density and plume temperature) relevant to laser ablation dynamics; in this respect, holographic techniques are particularly suitable for space and time-resolved measurements of plume dynamics.

3 Experimental realisation

The experimental setup shown in Figure 3 is used. The processing laser used is the Fianium HYLASE-25-SHG system (Fianium Ltd, Southampton, UK). The system operates at either λ=1064 nm or λ=532 nm, with a maximum pulse energy of E_{pulse}=125 µJ (in IR) and a pulse duration of τ_L<15 ps. Pulse trains are externally triggered via a BNC (TTL signal), capable of single-pulse operation up to a maximum repetition frequency of 40 MHz. For our process, we operated the laser in IR mode and used 10 pulses, each with E_{pulse}=48 µJ at a repetition rate of 500 kHz.

The laser pulse train is delivered to the sample by a Cambridge Technology Lightning II digital scanhead (Cambridge Technology, Planegg, Germany). A sample is placed on a moveable lab-jack and the position relative to the scan lens focal position is measured using a dial gauge. All experiments were carried with the focal position of the scanner lens coincident with the sample surface. After focusing using an 80-mm lens, the pulse train is delivered to the sample (into the page at element X in Figure 3). The resulting spot size is ≈30 µm to produce an energy density of ≈6.8 J cm^{-2} or a peak irradiance of ≈9×10^{11} W cm^{-2} per pulse.

To study the dynamical material response, a digital holographic imaging system was developed (Figure 3) (reported in [8, 15]). The imaging laser is a TEEM Photonics frequency doubled Q-switched PowerChip series platform (PNP-M08010, Edinburgh, Scotland) operating at λ=532 nm. The nominal pulse duration of the system is τ_L=400 ps. The system is capable of single-pulse operation to PRF$_{\text{max}}$=2.1 kHz. A Stanford Research Systems digital pulse generator (DG353, Sunnyvale, CA, USA) is used to trigger a single pulse. The pulse from the imaging laser is first cleaned using a spatial filter to produce a spatial TEM$_{00}$ Gaussian beam profile. It is then split using a polarising beam splitter (BS1) into the object and reference wave-carrier arms. The object arm is expanded

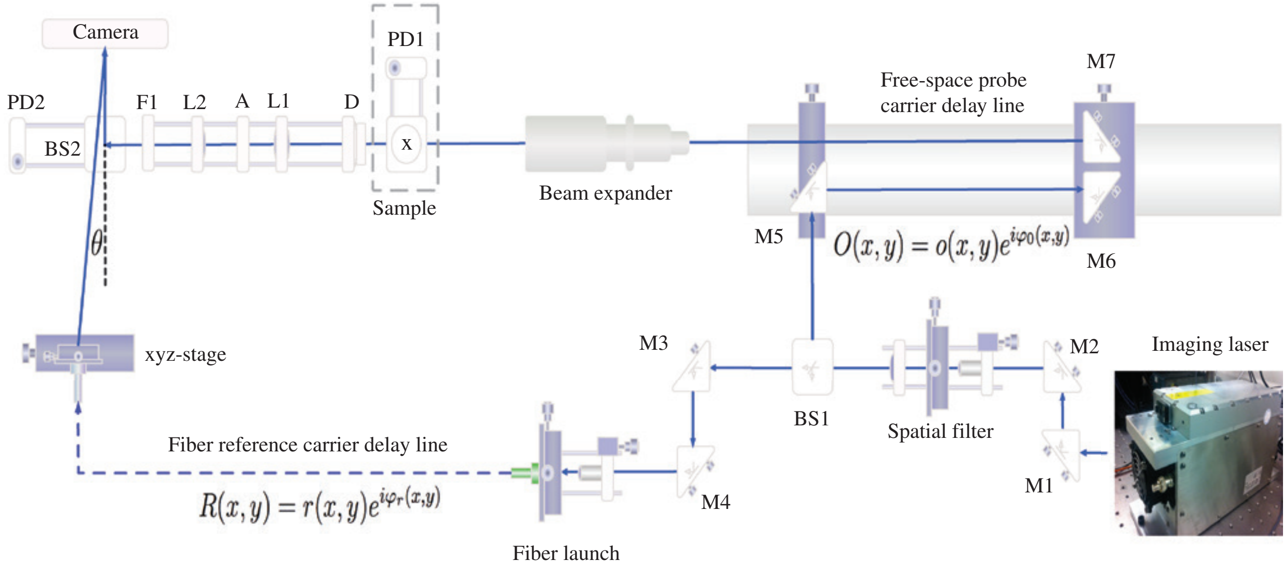

Figure 3: A top-down schematic view of the pulsed digital holographic interferometry system (bottom).

using a beam expander and propagated through the induced laser-induced ‘event’ at the sample (element X) and imaged directly onto the CCD chip using a 4f system (lenses L1, L2 and aperture A). The aperture (A) was adjusted to remove high spatial frequencies, which could not be resolved by the CCD. The field of view is chosen depending on the event under observation and appropriate optics, L1 and L2, selected. A narrow bandpass filter (λ=532 nm, FWHM=1 nm) was used to suppress plasma emission and luminescence. The reference arm is launched into a single-mode fibre and delivered through to the second beam splitter (BS2) prior to reaching the surface of the camera CCD chip. The camera is an iDS imaging µEye 3.0 Camera, 1/2″ CMOS sensor operated in global shutter mode, with 2.2 µm pixels. The temporal resolution of the system is limited by the pulse duration of the imaging laser. The object arm includes an optical delay line to ensure that the total path length difference between the object and reference arms is less than the coherence length of the imaging pulse, ≈10 mm. A photodiode (PD2) was used to determine the temporal overlap between the two reference arms, and the optical delay line was adjusted until there was good temporal overlap between the reference and object wavefronts, and clear interference fringes can be observed in the recorded image. The intensity of the two arms was equalised using the polarising beam splitter (BS1) to maximise fringe contrast and dynamic range recorded by the camera. The pattern observed by the camera is formed from interference of the light from the focal plane of L1 and the output of the reference carrier fibre, both of which originate at the same plane with respect to the CCD plane. The sample surface is positioned to coincide with the bottom of the field of view of the camera.

The pulse generator was used to trigger both the processing and imaging lasers sequentially, allowing for imaging throughout the event at different times by varying the pulse separation. For phase reconstruction, a minimum of two holograms are required. A Stanford Research Systems digital signal generator (DG353 model) was used to trigger the processing laser pulse-train and the holography system sequentially, thus, allowing imaging at any point in time during the processing up to 60 s in 1-ns steps.

3.1 Experimental procedure

The full process flow is presented in Figure 4. First, a reference hologram I_r, is taken without activating the processing laser; this captures the ambient background and acts as a reference. Additional object holograms $I_0(\Delta t)$ are acquired by triggering the camera at a time Δt after the impact of the processing pulse, (Figure 4A). Precise Δt measurements are ensured by integrated photodiodes (PD1 and PD2). A sequence of such images is acquired to produce a high-speed movie of the event, allowing visualisation of the full history of the event.

The phase difference is calculated by applying the Stetson formulation to one of the side lobes (Figure 4B, C), [16] whilst eliminating the random phase from the calculation as described by Saldner et al. [16] and Stetson [17]:

$$\Delta\varphi = tan^{-1}\frac{\mathbb{R}(\mathcal{F}_{FT}(I_0))\mathbb{I}(\mathcal{F}_{FT}(I_r)) - \mathbb{I}(\mathcal{F}_{FT}(I_0))\mathbb{R}(\mathcal{F}_{FT}(I_r))}{\mathbb{I}(\mathcal{F}_{FT}(I_0))\mathbb{I}(\mathcal{F}_{FT}(I_r)) + \mathbb{R}(\mathcal{F}_{FT}(I_0))\mathbb{R}(\mathcal{F}_{FT}(I_r))} \quad (5)$$

where $\mathbb{R}$ and $\mathbb{I}$ are the real and imaginary components of the Fourier Transformed $\mathcal{F}_{FT}$ image. After this operation, the effective pixel size is 11 µm in the reconstructed image.

3.1.1 Phase unwrapping: Phase changes in the object are typically continuous, but the Stetsons formula has a $\Delta\varphi=-\pi$ to π phase response leading to a wrapped phase image that must undergo an unwrapping procedure. There are many unwrapping algorithms that have been applied to phase problems in interferometry, and their methods and applications can be found in the key works by Stetson and Saldner [16], Kaufmann [18], Kemao [19] and Estrada [20], and references therein. All phase unwrapping in this work is implemented using the 2D-SRNCP [21, 22] phase unwrapper developed by Herraez et al., as shown in Figure 4D, E.

3.1.2 Backprojection: The resulting phase difference between the object and reference beam at any given location in the unwrapped

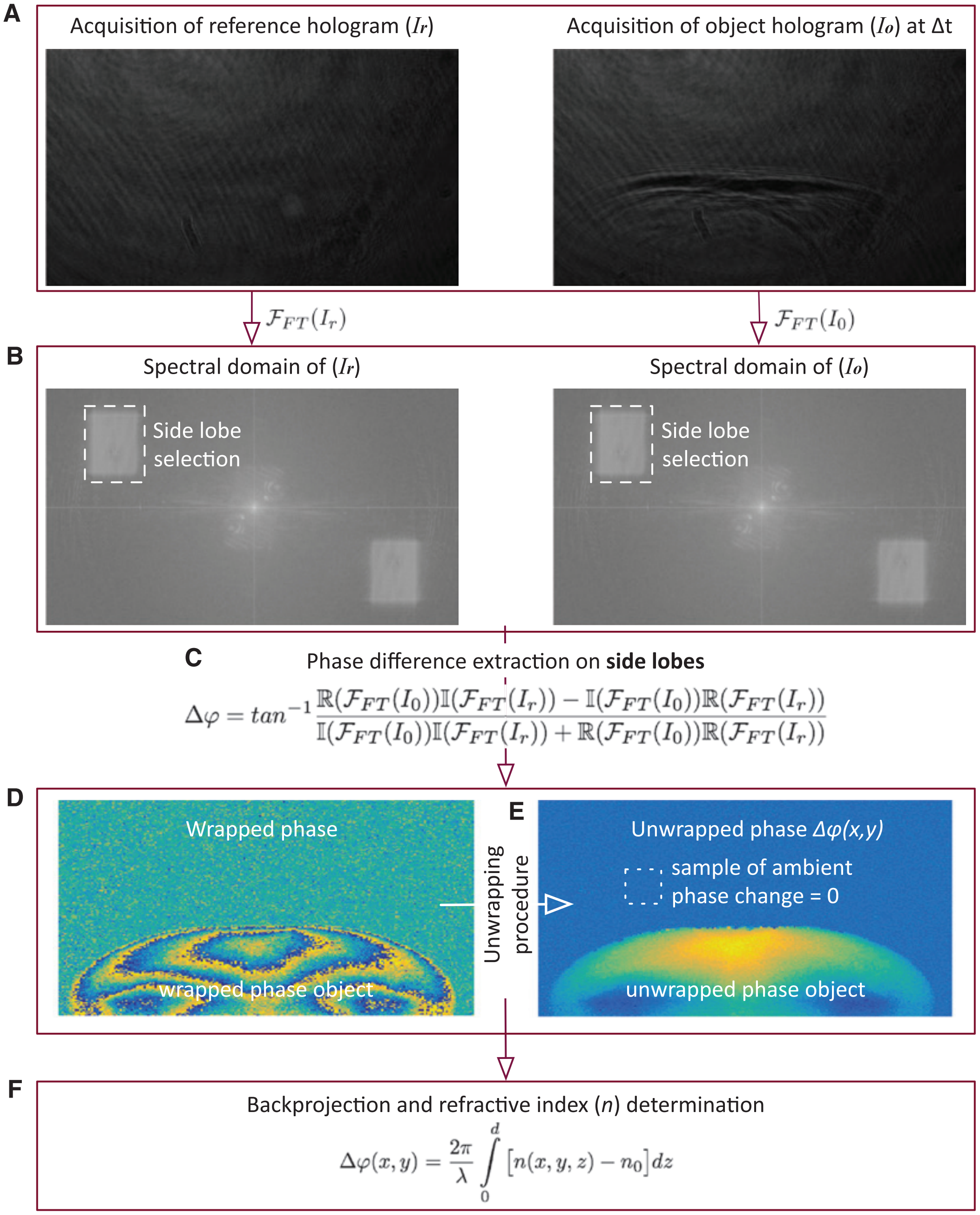

Figure 4: Diagrammatic representation of the process flow for image acquisition and reconstruction.

image represents the cord-integrated contribution as described in Eq. (4). As the 3D phase object is mapped onto a 2D plane, each point cannot be considered to be solely responsible for the detected phase change, and the refractive index cannot be arbitrarily determined from an unwrapped phase image; a further back-projection step is required.

The back-projection technique applied here relies on cylindrical symmetry of the object under observation. In the case of laser-induced shockwaves, this is a valid assumption, particularly when employing processing laser systems with a low M^2 (high beam quality) as this confines the shockwave-producing energy to a near-spherical geometry for low pulse numbers and cylindrical geometry with increased pulses on the sample surface.

The unwrapped image is disassembled into N slices perpendicular to the object symmetry, a single pixel wide. The single slice now gains a degree of symmetry about its centre, leading to spherical rotational symmetry. A MATLAB inverse discrete Radon transform is implemented to each nth slice using 180 separate projections with angular separation of 1°. This process disambiguates the phase contribution at each pixel by all other points along the photon trajectory. This process is repeated N times with each successive slice replaced with the back-projection.

3.1.3 Calculating the refractive index: Change in refractive index at any $(x, y)_z$ position requires knowledge of the total length, 0-*d*, over which the photon propagates and needs to be measured at each *n*th slice. The plume has cylindrical geometry with a defined edge (which determines the physical boundary of the object). As the absolute size of the object under observation is required, the field of view is measured using a negative U.S. Air Force target, and the object dimensions are determined by scaling the dimensions of the hologram and the unwrapped phase image for each slice. This way, the integral limits of Eq. (4) are determined for each backprojected slice. Applying Eq. (4) to the unwrapped, back-projected phase map yields the refractive index *change* at position (x, y) of the object (Figure 4F).

Finally, the background is sampled outside of the affected region and set to equal the refractive index of the ambient gas n_0. Adding this value to the refractive index change map gives the refractive index at any (x, y) position in the reconstructed image. More detail on phase unwrapping and back-projection techniques are discussed elsewhere [22–27]. Although not employed in this work, additional holographic reconstruction methods of interest to laser-material interaction diagnostics can be found elsewhere [12, 28–31].

3.1.4 Plume diagnostics: Holographic diagnostics of electron density does not require knowledge of absolute intensities and line shapes from emission lines. The method is based on the dependence of refractive index on electron density in the plasma plume. The contribution of free electrons to the refractive index can be assumed to dominate if the probing wavelength is chosen far from any absorption lines of the plasma. The refractive index maps are used to estimate the temperature and electron density of the plume and, consequently, to estimate pulse attenuation through the plume, and the amount of energy available at the sample surface.

The contribution of free electrons to the refractive index can be assumed to dominate if the *probing* wavelength is chosen far from any absorption lines of the plasma [11, 32, 33]. The electron density can be estimated by [14]:

$$N_e \simeq 10^{21}\lambda^{-2}(1-n^2) \tag{6}$$

for the case when $n<1$. The electron density is in cubic centimetres (cm^{-3}), and the wavelength is in micrometers. The temperature distribution in the plume is estimated by [34]:

$$T_p = \frac{T_0}{\left(\frac{n(x,y)-n_0}{n_0}\right)\left(\frac{3P_0A+2R_cT_0}{3P_0A}\right)+1} \tag{7}$$

where T_0 is the ambient temperature (assumed to be 300^0 K at n_0), $P_0=101.3$ kPa (kg m^{-1} s^{-2}) and γ is the ratio of specific heat capacities, $R_c=8.314$ J K^{-1} mol^{-1} is the molar gas constant and A is the molar refractivity of air. If the inverse brehmsstrahlung (IB) mechanism is the dominant mechanism, the penetration depth of a pulse through the plasma – analogous to penetration in materials – can be defined as [35]:

$$l_{IB} = a_c T_e^{3/2}(N_c/N_e)^2 \tag{8}$$

where T_e is the electron temperature, Eq. (7), in electron volts (eV), N_e is the electron density, from Eq. (6), and the wavelength-dependent critical plasma density $N_c=10^{21}/\lambda^2$ cm^{-3} in the case of $\lambda=1064$ nm [14, 35], where λ is the laser wavelength in micrometers. Once the characteristic penetration depth has been estimated, the total pulse energy loss after propagating a distance z through the plume, can be estimated by:

$$I(z) = I_0 e^{-z/l_{IB}} \tag{9}$$

where I_0 is the incident intensity, and $I(z)$ is the pulse intensity after propagating through a distance z through the plume. The IB characteristic absorption length is defined as $a_c=10^{-16}Z\ln\Lambda$, for ions of Ze electric charge where e is the electron charge, Z is the valance band charge number and $\ln\Lambda$ is the Coulomb logarithm [35, 36], where $\Lambda \simeq 5$ is the plasma parameter [37], for many laser-produced plasmas. The following assumptions and treatments are made:

- The events are treated as cylindrically symmetric about the incident laser beam axis, for the purposes of back-projection;
- The pulses are treated as δ functions with respect to the system;
- The temperature, electron density and absorption coefficient are calculated per pixel;
- When estimating the characteristic penetration depth of Eq. (8), we make the assumption that the plume temperature T_p from Eq. (7) and electron temperature T_e from Eq. (6) are in equilibrium, as the time each pulse spends propagating through each pixel $\simeq 4\times10^{-14}$ s; no appreciable temperature change occurs on this timescale;
- The total energy loss is calculated by applying Eq. (9) sequentially at each pixel (with z being the effective pixel size of 11 μm), determining the loss through that pixel and applying the result to each following pixel until the pulse has 'propagated' to the surface.

4 Results

Once a number of frames have been acquired and processed, diagnostic information of the process becomes available. Figure 5 shows the plume morphology at 1 μs after the 1st, 3rd, 6th and 10th pulse impacts during the process.

4.1 Plume dynamics

For the first pulse, the plume expands spherically for all tested materials, exhibiting Sedov-Taylor evolution [1, 2]. After the first pulse, the morphologies substantially deviate from the spherical model taking on characteristic shapes for each material, although all are characterised by a high degree of cylindrical symmetry.

Titanium exhibits multiple plasma regions that appear concurrently with the arrival of each pulse, at the crest of the pre-existing plume. Density analysis has shown that shockwave emission occurs simultaneously at the plume locus indicating line-geometry absorption, which is in-line with the beam propagation axis, and characterises multiple absorbing regions in the plume. Plume expansion likewise becomes highly elongated along the laser beam. At high pulse numbers, the plasma separates

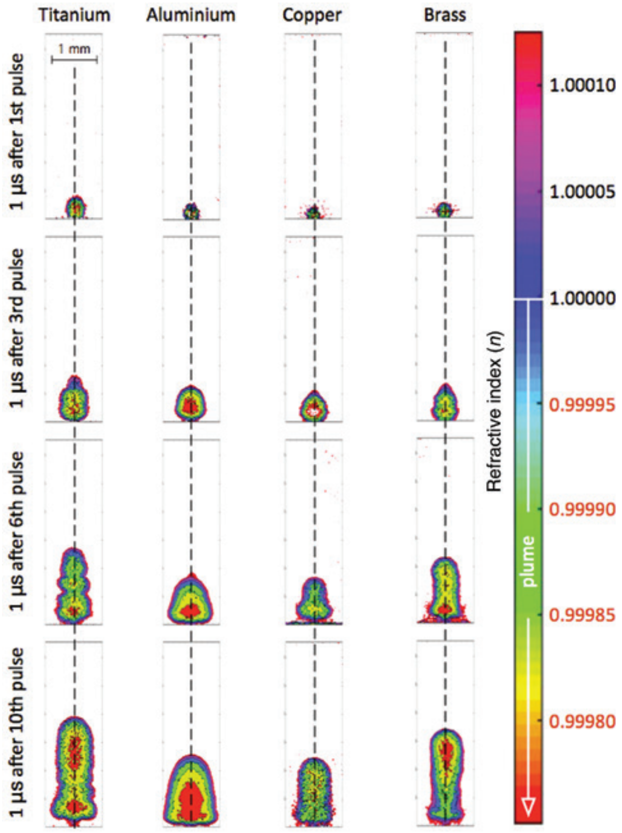

Figure 5: Plume morphology for each material at 1 µs after impact of the 1st, 3rd, 6th and 10th pulse in the pulse train. The field of view (FOV) in each image is x=1.2 mm by y=3.65 mm with the sample surface and laser focus situated at the bottom of the FOV. The dashed line in the images shows the laser beam axis.

from the surface, with only a limited zone near the surface connected with the plume, indicating that later pulses have limited effect on the sample.

Aluminium is characterised by a dense central plasma plume, which retains its original shape but grows with each additional pulse, contained in a single large volume.

Copper plume has the smallest volume and, over its lifetime, exhibits the lowest density. Like aluminium, copper only has a single region in which the plasma is generated but is highly irregular. At later times (after multiple pulses) copper also shows evidence of supra-surface interactions, similar to that reported in [4].

During early pulses, brass plasma morphology closely resembles that of the copper plume. It deviates from this behaviour at higher pulse numbers and takes on a similar morphology to titanium, characterised by a displacement of the plume from the surface, and secondary plasma regions further up the plume. Brass produces the densest plume of all the materials, which is consistent with multiple absorption lines [11] from both copper and zinc, which would give rise to multiple ionic species.

In all cases, it must be noted that the focal spot represents about 3 pixels on each image, demonstrating the size of the plume in relation to the sample interaction zone. Application of Eq. (6) to data in Figure 5 shows that at the plume centres, the electron density can reach as high as $N_e \simeq 10^{18}$ cm^{-3}, which is consistent with high peak power picosecond interactions with metals, shown in Figure 6.

4.2 Optimising the process for maximum energy delivery to the sample

Applying the treatment described in Sections 3.1.4 shows that any subsequent pulses are attenuated to ≃53%, ≃43%, ≃62% and ≃31% of their original values after passing through the centre of the titanium, aluminium, copper and brass plumes, respectively – prior to reaching the sample. In the context of surface-structuring operations. it is apparent that these dynamics play an important role on the process. Two optimisation strategies, to maximise pulse energy delivery to the sample, are now available to counter the dynamic effects:

- Energy delivery optimisation based on plume dissipation: First, it is possible to allow a sufficient amount of time for the plume to dissipate to an acceptable level. The refractive index is sampled 300 µm above the sample surface showing that a plume is still present (i.e. $n \neq n_{ambient}$) as late as 24 µs after the process starts for each material. The plume does fully not dissipate until 100s of µs later, which would fall well within the processing window of the next pulse train. Waiting for the plume to dissipate completely would require the process to be slowed down considerably, which is typically not an industrially relevant option for lasers operating at repetition rates higher than a few tens of kHz, assuming comparable energy densities.
- Energy delivery optimisation based on beam displacement: Alternatively, the beam can be displaced to avoid the plume altogether; we set a condition that any subsequent pulse train must not pass through the plume so as to avoid being attenuated or defocused. This is to ensure that a consistent machining outcome is achieved, while maximising the duty cycle of the operation; the data in Figure 5 is then directly used to identify the minimum lateral beam displacement $\Delta\vec{X}{=}{\simeq}570\ \mu\text{m}$ at which there is no plume is detected, i.e. $\Delta\varphi=0$ in Eq. (4). In this example, a time of 1 µs after each pulse is examined corresponding to a processing laser operating at a pulse repetition rate of

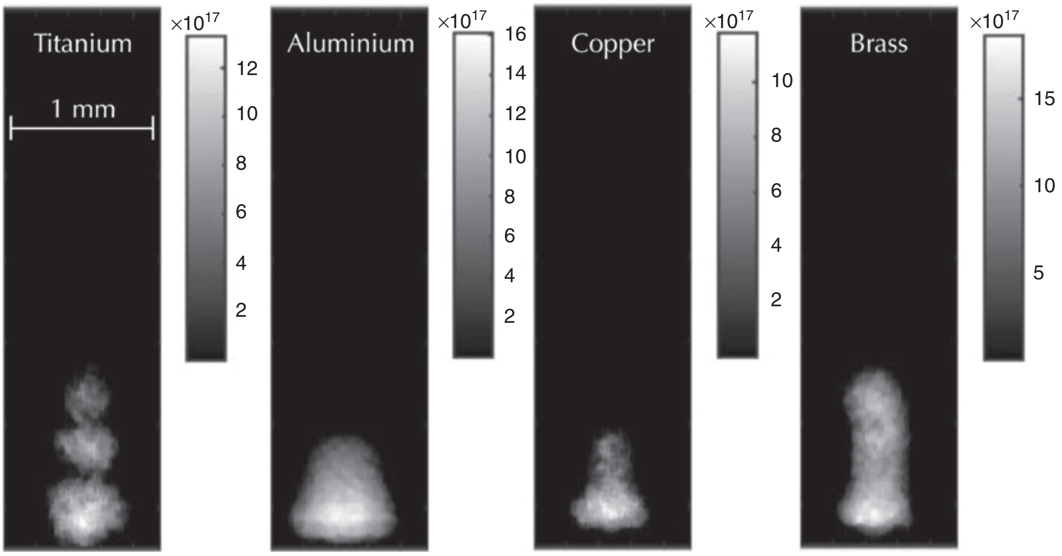

Figure 6: Electron density ($e^{-}cm^{-3}$) distributions for titanium, aluminium, copper and brass imaged 1000 ns after the 6th pulse impact.

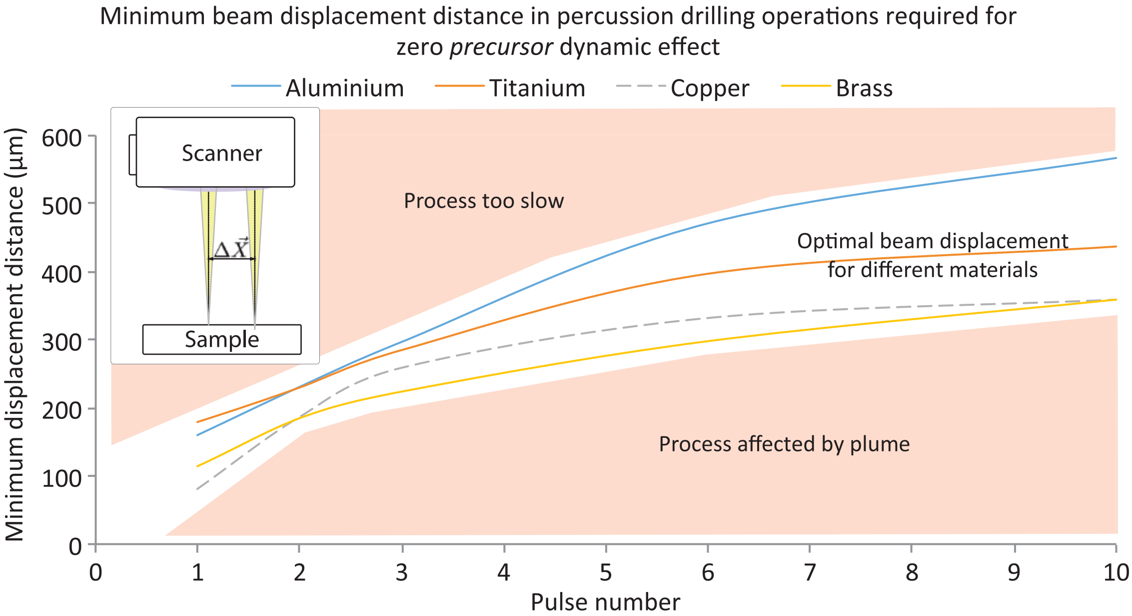

Figure 7: Lateral beam displacement required for a zero precursor dynamic effect. Inset shows the general geometry employed when considering required displacement distance $\Delta\vec{X}$.

1 MHz. Displacements required to satisfy our condition are shown in Figure 7 for the tested materials. At 1 µs after 10 pulses, the lateral plume size is largest for aluminium, requiring a displacement of $\Delta\vec{X}$=330 µm in any direction radially away from the plume centre, to completely avoid the plume. Titanium also produces a wide plume, with a cylindrical radius at its widest point of ≃440 µm. Although brass produces an elongated plume, it is radially comparable to copper requiring the beam to be displaced by ≃360 µm to avoid *any* supra-surface dynamic effects.

In this example, we have made our processing condition very harsh; no part of the beam is allowed to pass through the plume. However, it has to be noted that the energy penalty for clipping the plume is not as severe, as say going straight through the centre as we have done here; although moving to the edge of a plume may introduce other refractive index-induced effects, depending on the size and composition of the plume. In the case of six pulses on aluminium, for example, if the beam was displaced by $\Delta\vec{X}.$ instead of completely avoiding the plume, the incident pulse would be attenuated to ≃72% of its original value compared to ≃43% at the centre of the plume. Using data such as presented in Figure 7, the industrial laser user able to make a direct assessment of minimum beam displacement to optimise (maximise) pulse energy delivery to the sample, depending on required throughput, post-process precision and on what degree of energy loss is acceptable.

5 Conclusion

We have presented our account of the problems associated with an empirical approach to laser-material process design and presented an alternative methodology based on ultrafast holography. An account of the basics of holography has been given, in the context of laser-material interaction diagnostics. Methods for interpreting holographic data for use for diagnosing laser materials processing operations have been provided.

The methodology described here allows industrial laser users to characterise their processes and gives them an opportunity to optimise the entire operation based on direct, quantitative evidence, thus, rendering an empirical parameter sweep unnecessary. The recorded process dynamics were used to propose two optimisation strategies: first, by observing the time at which the plume fully dissipates and, second, through calculation of the minimum beam displacement required to maximise energy delivery to the sample by avoiding the plume. We have applied this methodology to a simple case of maximising energy delivery to the sample in a surface-structuring process and provided what we believe to be the first attempt to optimise a process with respect to energy delivery using digital holographic interferometry.

The general tenets of the method could be extended to optimise laser shock peening, cutting, welding or percussion drilling operations. It is equally possible to use the described methods to improve operations containing many more pulses or even apply these techniques to design optimal pulse shapes [8].

Acknowledgments: This work was carried out under EPSRC grant number EP/K030884/1, as part of the EPSRC Centre for Innovative Manufacturing in Laser-based Production Processes. The authors would like to extend their gratitude to their colleagues at Applied Laser Engineering Ltd, UK, for their kind support of this work.

References

[1] G. Taylor, Proceedings of the Royal Society A: Mathematical, Physical and Engineering Sciences, 201, 159–174 (1950).
[2] G. Taylor, Proceedings of the Royal Society A: Mathematical, Physical and Engineering Sciences, 201, 175–186 (1950).
[3] O. Yavas, E. L. Maddocks, M. R. Papantonakis and R. F. Haglund Jr., Appl. Surf. Sci. 127, 26–32 (1998).
[4] S. S. Mao, X. Mao, R. Greif and R. E. Russo, J. Appl. Phys. 89, 4096 (2001).
[5] S.-B. Wen, X. Mao, R. Greif and R. E. Russo, J. Appl. Phys. 101, 023115 (2007).
[6] N. M. Bulgakova and A.V. Bulgakov, Appl. Phys. A Mater. Sci. Process. 73, 199–208 (2001).
[7] J. H. Yoo, S. H. Jeong, X. L. Mao, R. Greif and R. E. Russo, Appl. Phys. Lett. 76, 783 (2000).
[8] K. Pangovski, M. Sparkes, A. Cockburn, W. O'Neill and D. Richardson, IEEE J. Sel. Top. Quantum Electron. 20, 51–63 (2014).
[9] J. W. Goodman and R. W. Lawrence, Appl. Phys. Lett. 77, 11 (1967).
[10] E. N. Leith and J. Upatnieks, J. Opt. Soc. Am. 52, 1123–1130 (1962).
[11] S. Amoruso, R. Bruzzese, N. Spinell and R. Velotta, J. Phys. B: At. Mol. Opt. Phys. 32, R131–163 (1999).
[12] U. Schnars and W. P. O. Jüptner, Meas. Sci. Technol. 13, 13 (2002).
[13] E. Amer, P. Gren and M. Sjödahl, J. Phys. D: Appl. Phys. 41, 215502 (2008).
[14] E. Amer, P. Gren and M. Sjödahl, Opt. Lasers Eng. 47, 793–799 (2009).
[15] A. G. Demir, K. Pangovski, W. O'Neill and B. Previtali, J. Phys. D: Appl. Phys. 48, 235202 (2015).
[16] H. O. Saldner, N. E. Molin and K. A. Stetson, Appl. Opt. 35, 332–336 (1996).
[17] K. A. Stetson and W. R. Brohinsky, Appl. Opt. 24, 3631 (1985).
[18] G. H. Kaufmann and G. E. Galizzi, Appl. Opt. 41, 7254–7263 (2002).
[19] Q. Kemao. Opt. Lasers Eng. 45, 304–317 (2007).
[20] J. C. Estrada, M. Servin and J. Vargas, Opt. Lasers Eng. 50, 1026–1029 (2012).
[21] M. A. Herraez, M. A. Gdeisat, D. R. Burton and M. J. Lalor, Appl. Opt. 41, 7445–7455 (2002).
[22] M. A. Herraez, D. R. Burton, M. J. Lalor and M. A. Gdeisat, Appl. Opt. 41, 7437–7444 (2002).
[23] M. A. Herráez, M. A. Gdeisat, D R Burton and M. J. Lalor, Appl. Opt. 41, 7445–7455 (2002).
[24] U. Schnars and W. Juptner, Meas. Sci. Technol. 13, 3228–3235 (2002).
[25] P. Gren, S. Schedin and X. Li, Appl. Opt. 37, 834–840 (1998).
[26] E. Amer, P. Gren, A. F. H. Kaplan and M. Sjödahl, Appl. Surf. Sci. 255, 8917–8925 (2009).
[27] S. Grilli, P. Ferraro, S. De Nicola, A. Finizio, G. Pierattini and R. Meucci, Opt. Express 9, 294–302 (2001).
[28] N. Verrier and M. Atlan, Appl. Opt. 50, H136–H146 (2011).
[29] J. Li, P. Tankam, Z. Peng and P. Picart, Opt. Lett. 34, 572–574 (2009).

[30] P. Picart, P. Tankam, D. Mounier, Z. Peng and J. Li, Opt. Lett. 17, 9145–9156 (2009).
[31] L. I. Bluestein, IEEE Trans. Audio Electroacoustics 18, 451–455 (1970).
[32] H. R. Griem. ‘Plasma Spectroscopy’, (McGraw-Hill, New York, 1964).
[33] D. Breitling, H. Schittenhelm, P. Berger, F. Dausinger and H. Hügel, Appl. Phys. A: Mater. Sci. Process. 69, S505–S508 (1999).
[34] S. Sharma, G. Sheoran and C. Shakher, Appl. Opt. 51, 3228 (2012).
[35] M. Stafe, C. Negutu and I. M. Popescu, Shock Waves 14, 1–4 (2005).
[36] T. W. Murray and J. W. Wagner, J. Appl. Phys. 85, 2031 (1999).
[37] J. D. Huba, NRL PLASMA FORMULARY Supported by The Office of Naval Research. Office of Naval Research, pages 1–71, 2009.

Krste Pangovski
Centre for Industrial Photonics, Institute for Manufacturing, University of Cambridge
CB30FS, UK
kp358@cam.ac.uk

Krste Pangovski obtained his BSc in 2004 and MSc in 2005 in Physics. Following his degrees, he moved into Business Technology Research and Development, operating within the areas of Strategy, Business Development and Design. In 2009, Krste returned to pursue his academic interests by undertaking an MRes in Photonic Systems Development concentrating on Industrial Laser design. After completing his doctoral work ‘Nanosecond control of material transport in laser ablation’ at the University of Cambridge, he joined the Centre for Industrial Photonics as a research associate, concentrating on diagnostics of laser-material interactions.

Martin Sparkes
Centre for Industrial Photonics, Institute for Manufacturing
University of Cambridge, CB30FS, UK

Martin Sparkes obtained his MEng in Mechanical Engineering from The University of Liverpool in 1991. In 2003, he moved to Cambridge to be part of the Centre for Industrial Photonics. Martin is a Senior Research Associate within the Cambridge University Engineering Department funded on the EPSRC Centre for Innovative Manufacturing in Ultra Precision project.

William O’Neill
Centre for Industrial Photonics, Institute for Manufacturing
University of Cambridge, CB30FS, UK

William O’Neill is a Professor of Laser Engineering within the Cambridge University Engineering Department and Director of the Centre of Industrial Photonics. He has written over 170 research publications and scientific papers on the subject of laser-matter interactions, optical engineering, laser-based manufacturing technologies and micro/nano fabrication techniques. He is a member of the international advisory panel of the National Laser Centre of South Africa, a Director of the Laser Institute of America, and advises industry on a number of laser-based manufacturing technologies.